

# Use of near-real-time satellite precipitation data and machine learning to improve extreme runoff modeling

Paul Muñoz<sup>1</sup>, Gerald Augusto Corzo Perez<sup>2</sup>, Dimitri Solomatine<sup>3</sup>, Jan Feyen<sup>4</sup>, and Rolando Céleri<sup>1</sup>

<sup>1</sup>Universidad de Cuenca

<sup>2</sup>UNESCO-IHE Institute for Water Education

<sup>3</sup>UNESCO-IHE Delft Institute for Water Education

<sup>4</sup>Katholieke Universiteit Leuven

November 22, 2022

## Abstract

Extreme runoff modeling is hindered by the lack of sufficient and relevant ground information and the low reliability of physically-based models. The authors propose to combine precipitation Remote Sensing (RS) products, Machine Learning (ML) modeling, and hydrometeorological knowledge to improve extreme runoff modeling. The approach applied to improve the representation of precipitation is the object-based Connected Component Analysis (CCA), a method that enables classifying and associating precipitation with extreme runoff events. Random Forest (RF) is employed as a ML model. We used 2.5 years of nearly-real-time hourly RS precipitation from the PERSIANN-CCS and IMERG-early run databases (spatial resolutions of 0.04 o and 0.1 o , respectively), and runoff at the outlet of a 3391 km<sup>2</sup>-basin located in the tropical Andes of Ecuador. The developed models show the ability to simulate extreme runoff for the cases of long-duration precipitation events regardless of the spatial extent, obtaining Nash-Sutcliffe efficiencies (NSE) above 0.72. On the contrary, we found an unacceptable model performance for a combination of short-duration and spatially-extensive precipitation events. The strengths/weaknesses of the developed ML models are attributed to the ability/difficulty to represents complex precipitation-runoff responses.

# Use of near-real-time satellite precipitation data and machine learning to improve extreme runoff modeling.

Paul Muñoz<sup>1,2</sup>, Gerald Corzo<sup>3</sup>, Dimitri Solomatine<sup>3</sup>, Jan Feyen<sup>4</sup>, and Rolando Célleri<sup>1,2</sup>.

<sup>1</sup> Departamento de Recursos Hídricos y Ciencias Ambientales, Universidad de Cuenca, Cuenca 010150, Ecuador.

<sup>2</sup> Facultad de Ingeniería, Universidad de Cuenca, Cuenca 010150, Ecuador.

<sup>3</sup> Hydroinformatics Chair Group, IHE Delft Institute for Water Education, 2611 AX Delft, The Netherlands.

<sup>4</sup> Faculty of Bioscience Engineering, Catholic University of Leuven, Leuven 3001, Belgium.

## Abstract

Extreme runoff modeling is hindered by the lack of sufficient and relevant ground information and the low reliability of physically-based models. The authors propose to combine precipitation Remote Sensing (RS) products, Machine Learning (ML) modeling, and hydrometeorological knowledge to improve extreme runoff modeling. The approach applied to improve the representation of precipitation is the object-based Connected Component Analysis (CCA), a method that enables classifying and associating precipitation with extreme runoff events. Random Forest (RF) is employed as a ML model. We used 2.5 years of nearly-real-time hourly RS precipitation from the PERSIANN-CCS and IMERG-early run databases (spatial resolutions of 0.04° and 0.1°, respectively), and runoff at the outlet of a 3391 km<sup>2</sup>-basin located in the tropical Andes of Ecuador. The developed models show the ability to simulate extreme runoff for the cases of long-duration precipitation events regardless of the spatial extent, obtaining Nash-Sutcliffe efficiencies (NSE) above 0.72. On the contrary, we found an unacceptable model performance for a combination of short-duration and spatially-extensive precipitation events. The strengths/weaknesses of the developed ML models are attributed to the ability/difficulty to represents complex precipitation-runoff responses.

**Keywords:** Extreme runoff; Machine Learning; PERSIANN-CCS; IMERG-early-run; Feature Engineering; Tropical Andes.

## 19        **1. Introduction**

20    Physically-based precipitation-runoff models used in water management describe the physical  
21    processes that occur in a system (basin) by using balance and conservation equations (Clark et  
22    al., 2017). However, those models demand extensive data and might be subject to  
23    overparameterization, limiting its operational value (Mosavi et al., 2018; Young, 2002). As a  
24    solution, during the last decades, a data-driven approach, using Machine Learning (ML)  
25    techniques, gained popularity among hydrologists (Bontempi et al., 2012; Chang et al., 2019;  
26    Galelli and Castelletti, 2013; Mosavi et al., 2018). An important reason responsible for the  
27    increasing interest is the fact that ML exploits the available and relevant information (e.g.,  
28    precipitation, past runoff) to find relations to the target variable (i.e., runoff) without requiring  
29    knowledge about the underlying physical processes. Among ML techniques, the Random  
30    Forest (RF) algorithm is mostly used for normal and extreme runoff modeling due to its  
31    simplicity (few parameters to calibrate), higher accuracy when compared to other ML  
32    techniques, the robustness of the model, and its capacity to deal with small size samples and  
33    complex data structures (Biau and Scornet, 2016; Breiman, 2001; Contreras et al., 2021; Li et  
34    al., 2016a; Li et al., 2020; Muñoz et al., 2018, 2021; Orellana-Alvear et al., 2020;  
35    Papacharalampous and Tyrallis, 2018; Tyrallis et al., 2019; Wang et al., 2015).

36    In terms of data availability, in many regions, ground precipitation networks are either  
37    inexistent or scarce, and if available mostly with extremely low areal density. This is especially  
38    true for mountainous regions, such as the tropical Andes, where the remoteness of the study  
39    areas and budget constraints limits the development of accurate precipitation-runoff models.  
40    Fortunately, continuous development of Remote Sensing (RS) products, e.g., space-based  
41    satellites have dramatically enhanced the quantity (spatiotemporal resolution) and quality of  
42    areal precipitation observations. However, RS precipitation obtained from a single sensor  
43    (satellite) hardly provides accurate estimations (Hong et al., 2019). This has stimulated the

44 development of multi-satellite precipitation products such as the NASA Global Precipitation  
45 Measurement (GPM) Integrated Multi-satellitE Retrievals for GPM (IMERG) (Huffman et al.,  
46 2015), and the Precipitation Estimation from Remotely Sensed Information using Artificial  
47 Neural Networks (PERSIANN) (Hsu et al., 1997). IMERG and PERSIANN products are  
48 characterized by quasi-global coverage, free access, high spatiotemporal resolutions, and in  
49 continuous development (Tang et al., 2016). Given previous, both RS products are nowadays  
50 widely used in hydrometeorological applications including tracking of precipitation anomalies  
51 (Nguyen et al., 2014; Sakib et al., 2021), precipitation early-warning systems (Sorooshian et  
52 al., 2014), and flood forecasting and mapping (Belabid et al., 2019; Nguyen et al., 2015).

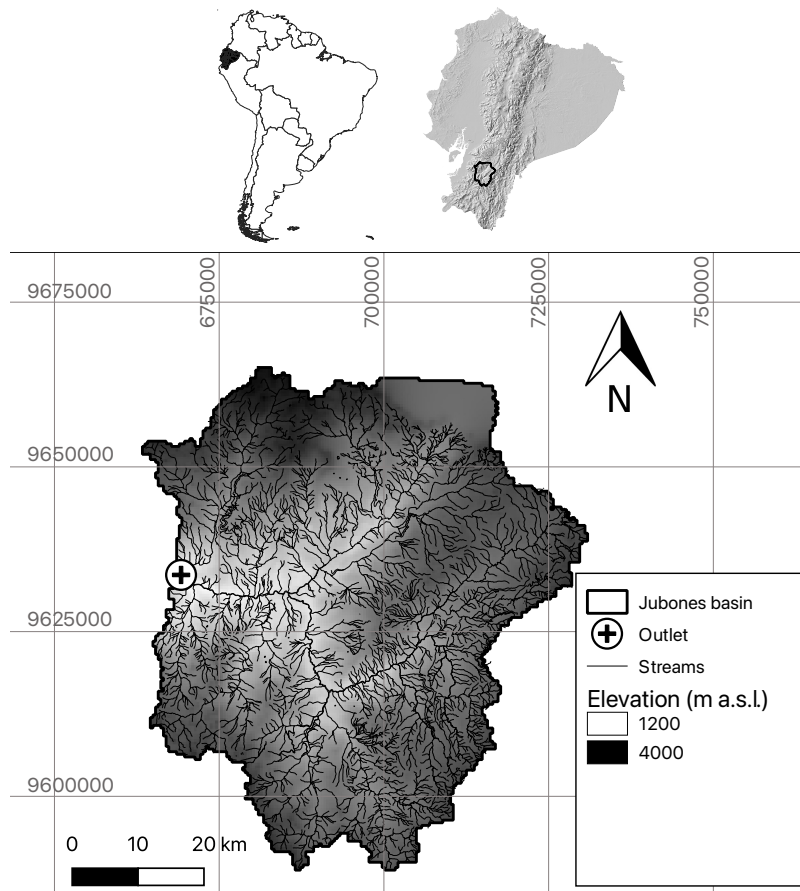
53 Once the issue of data availability is solved the arising research questions are: a) is precipitation  
54 well represented by RS data? and b) can RS precipitation be properly assimilated during the  
55 learning process (in the context of extreme runoff ML models)? The first research question is  
56 mandatory for the cases when the interest lies in providing accurate precipitation estimations.  
57 This can be achieved by validating RS products with ground precipitation estimations, see for  
58 instance the studies of Laverde-Barajas et al. (2019) and (Li et al., 2016b). While, the second  
59 issue can be addressed regardless the validation of the precipitation, for the cases when  
60 precipitation is merely an estimator for the modeling of another variable (e.g., precipitation is  
61 an estimator in precipitation-runoff models). In this case, the methodology consists of applying  
62 a feature engineering strategy to RS precipitation data enabling a better ML precipitation  
63 assimilation during the learning process, improving ultimately extreme runoff model  
64 efficiencies. In addition, ML precipitation assimilation can be improved by building runoff  
65 models able to discriminate between different precipitation event types (Laverde-Barajas et al.,  
66 2020). This is because different precipitation events produce different runoff responses as a  
67 result of various runoff generation processes, mainly infiltration and saturation excess  
68 (Gutiérrez-Jurado et al., 2019).

69 Precipitation events can be distinguished by applying object-based methods to RS imagery  
70 (Davis et al., 2006; Laverde-Barajas et al., 2019; Li et al., 2016b; Peña-Barragán et al., 2011;  
71 Vogels et al., 2020). A simple yet effective object-based method is the Connected Component  
72 Analysis (CCA) employed by Laverde-Barajas et al. (2019). The CCA includes a physical  
73 description of precipitation events (centroid, extension area, etc.), as well as key meteorological  
74 attributes (intensity, duration, volume, etc.). These characteristics are then used for classifying  
75 precipitation events which can be contrasted with their associated runoff responses.  
76 In this context, the objective of this study was to develop specialized (smart) ML extreme  
77 runoff models for a 3393-km<sup>2</sup> basin in Ecuador. We used a feature engineering methodology  
78 to improve the areal representation of the precipitation and to maximize runoff model  
79 efficiencies by identifying and classifying precipitation events associated with extreme  
80 hydrological events.

## 81 **1. Study area and Dataset**

### 82 1.1 Study area

83 The Jubones Basin, located in the tropical Andes of Ecuador, was selected as the study area  
84 (Figure 1) and covers an area of ~3391 km<sup>2</sup> upstream of the Minas-San Francisco hydroelectric  
85 dam, with an elevation ranging between 1250 to 3920 m above sea level. The climatology of  
86 the basin is extremely variable due to the presence of the Andean mountain range, trade winds,  
87 and ocean currents from the Pacific Ocean. A distinction can be made between at least 4 rainfall  
88 regions, including a semi-arid region. The basin climate ranges from humid to arid, with  
89 average annual rainfall ranging spatially from 350 to 1170 mm.



91 Figure 1. The Jubones basin in the Tropical Andes of Ecuador, South America.

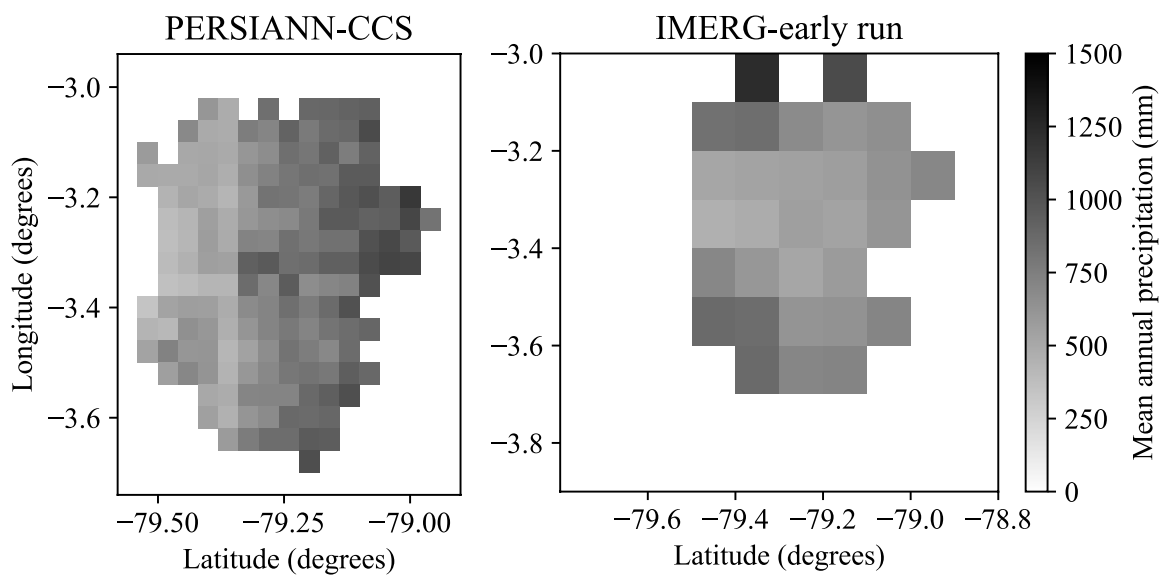
## 92 1.2 Dataset

93 The dataset comprises hourly satellite-derived precipitation covering the Jubones basin, and  
 94 hourly runoff data collected at the hydrological station, situated in the outlet of the basin,  
 95 consisting of the Minas-San Francisco hydropower dam. Since the dam was completed in 2018,  
 96 lasted the study period  $\sim 2.5$  years, from 18 November 2018 to the 31<sup>st</sup> of March 2021.

### 97 *Precipitation from Remote Sensing (RS) products*

98 Precipitation information was retrieved from two near-real-time multi-satellite sources, the  
 99 IMERG-early run, and the PERSIANN-Cloud Classification System (CCS) precipitation  
 100 subproducts. Data were derived at hourly intervals. The main difference between both  
 101 precipitation sources is the spatial resolution. The PERSIANN-CCS possesses the highest  
 102 spatial resolution for the region ( $0.04^\circ \times 0.04^\circ$ ), being the result of infrared imagery processing

103 and cloud classification using artificial neuronal networks (Hong et al., 2004). Whereas the  
 104 IMERG-early run approach interpolates various microwave precipitation estimates and  
 105 delivers data with a spatial resolution of  $0.1^\circ \times 0.1^\circ$ .  
 106 Figure 2 shows the mean annual precipitation of the Jubones basin, measured by the  
 107 PERSIANN-CCS (728.5 mm) and IMERG-early run (727.2 mm) precipitation satellite  
 108 subproducts. For this plot, we used hourly information for 2019 and 2020 (see also the  
 109 precipitation plot in Figure 3). We found differences of 1.3 and 116 mm between the mean and  
 110 the maximum annual precipitation obtained from the PERSIANN-CCS and the IMERG-early  
 111 run subproducts, respectively. This is attributed to the spatial resolution difference and to the  
 112 measurement principle of each satellite subproduct.

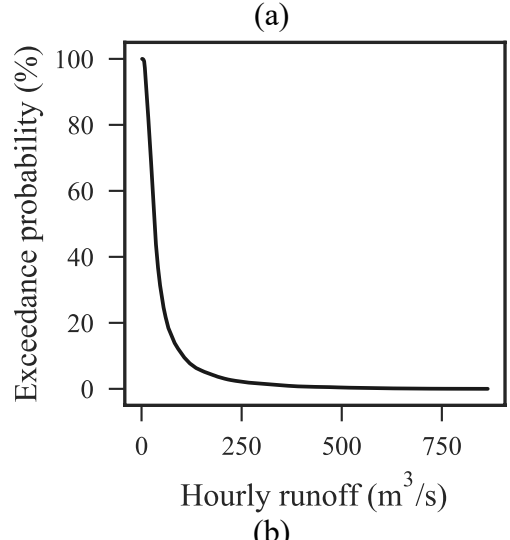
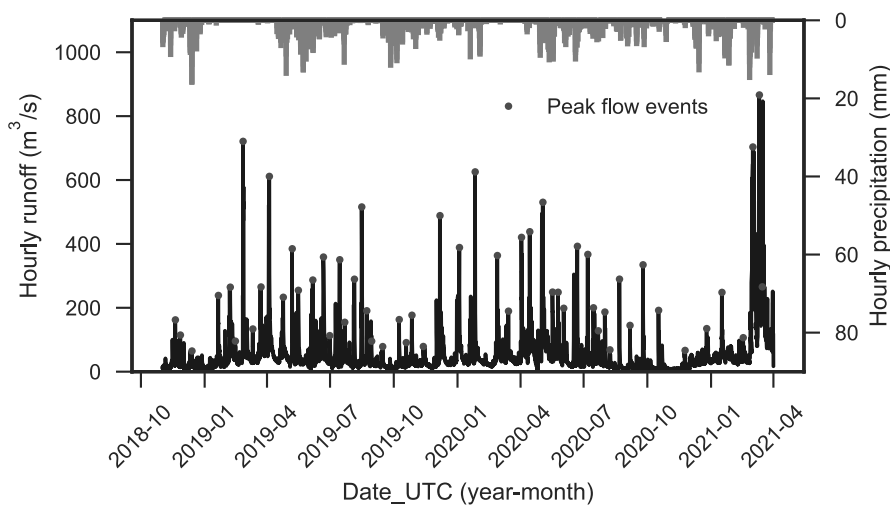


113 Figure 2. Mean annual precipitation in mm (2019 and 2020) measured by the PERSIANN-  
 114 CCS and the IMERG-early run precipitation satellite subproducts.  
 115

116 *Runoff at the entrance of the MSF hydropower dam*

117 Hourly time series of runoff at the outlet of the Jubones basin were derived from the server of  
 118 the Corporación Eléctrica del Ecuador (CELEC EP, <https://www.celec.gob.ec/>), the company  
 119 that manages the Minas-San Francisco hydropower dam. Figure 3 depicts the runoff  
 120 information for the study period. Figure 3a shows the hourly time series, whereas Figure 3b

121 the corresponding probability of exceedance from which 55 nearly-independent peak flow  
 122 events were selected based on peak-over-threshold values (red dots in Figure 3a). The peak  
 123 flow events selection was done using the WETSPRO tool (Willems, 2009). Exceedance  
 124 probability analysis reveals that for the study period the runoff magnitudes of 103.5 and 159.4  
 125  $\text{m}^3 \cdot \text{s}^{-1}$  are exceeded with probabilities of 10% and 5%, respectively. These probabilities, which  
 126 correspond to the 90 and 95% quartiles, served to determine extreme hydrological runoff events  
 127 for the development of the extreme precipitation-runoff models.



128 Figure 2. (a) Runoff and precipitation (PERSIANN-CCS) time series at the outlet of the  
 129 Jubones basin. Peak flow events are displayed as red dots. (b) Exceedance probability for the  
 130 study period (18/11/2018 to 31/03/2021).  
 131

132

## 133 2. Methodology

### 134 2.1 Determination of nearly independent peak hydrological events

135 The extreme hydrological events from the complete runoff time series were derived by  
136 applying the following two criteria: i) extreme hydrological events must exceed the 90%  
137 quartile values ( $98.8 \text{ m}^3 \cdot \text{s}^{-1}$ ), and ii) such events must be nearly independent. For meeting both  
138 criteria of independence, we used the WETSPRO time series tool (Willems, 2009), which splits  
139 runoff series in nearly independent peak and low flow events following a peak-over-threshold  
140 approach. The WETSPRO has two parameters to be calibrated, the inter-event time and peak  
141 height. In summary, we selected extreme hydrological events with a definition of independence  
142 controlled by the recession time and peak height difference of two consecutive runoff events.

### 143 2.2 Object-based Connected Component Analysis

144 Once extreme hydrological events were selected, the next step was to analyze their  
145 correspondent precipitation imagery from the highest-resolution satellite subproduct, the  
146 PERSIANN-CCS. The precipitation analysis was done by applying a feature engineering  
147 strategy based on an object-based Connected Component Analysis (CCA) algorithm. The CCA  
148 algorithm is fully detailed in Laverde-Barajas et al. (2019). We implemented the CCS  
149 algorithm through the scikit-image processing package in Python® version 3.7 (der Walt et al.,  
150 2014). The approach consists of the following steps (see also Figure 4):

- 151 i. Clipping of the precipitation imagery to the Jubones basin (Figure 4a).
- 152 ii. Identification and localization of precipitation objects (latitude, longitude, see  
153 Figure 4b). For this we defined a precipitation threshold volume of 0.5 mm, i.e.,  
154 precipitation objects with an associated precipitation volume of less than 0.5 mm  
155 are trimmed-off. This was done on a trial-and-error basis validated with  
156 precipitation objects observed in randomly selected precipitation events. The target

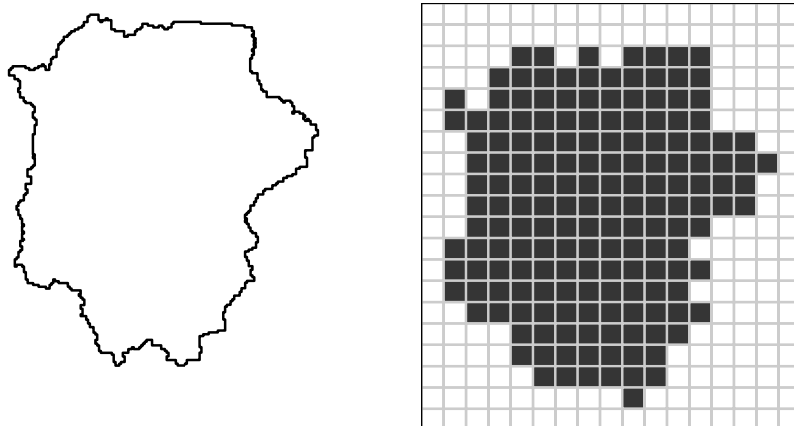
157 was to remove noise from precipitation imagery and keep only clear precipitation  
158 objects in the precipitation imagery (Figure 4c).

159 iii. Filtering of the identified precipitation objects according to size criteria. Similarly,  
160 we found and used a number-of-pixels threshold of 6, according to a trial-and-error  
161 procedure with the same target as employed in step (ii).

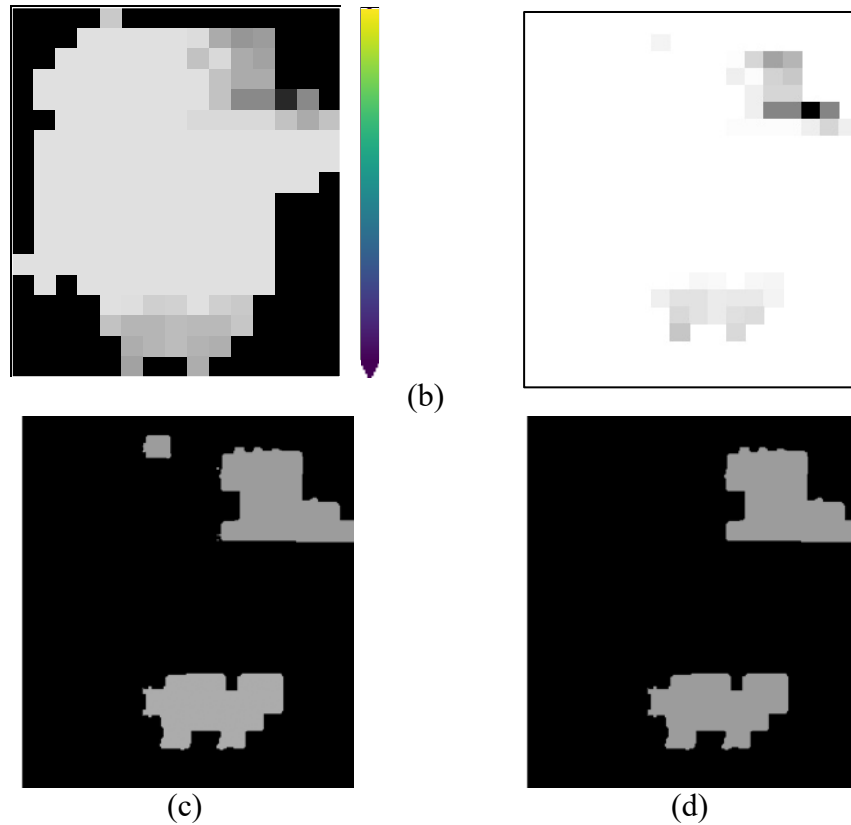
162 iv. Morphologically the identified and filtered precipitation objects were closed, by .  
163 applying as a final procedure a dilatation-and-erosion algorithm for refining  
164 precipitation objects (Figure 4d).

165 v. Retrieval of physical (centroid and extension area) and hydrometeorological  
166 attributes (volume of precipitation, maximum intensity, precipitation duration)  
167 from the precipitation objects defined in step (iv). For the duration of the  
168 precipitation, we defined that two precipitation objects are considered consecutive  
169 (i.e., belong to the same event) when the time between their appearance is shorter  
170 than 2 hours. This threshold was calibrated on a trial-and-error basis.

171



(a)



172 Figure 3. Precipitation identification with an object-based Connected Component Analysis  
 173 Illustration of the PERSIAN-CCS 2021-12-25 05:00 UTC image. (a) Jubones basin clipping,  
 174 (b) Precipitation identification in mm from PERSIANN-CCS imagery, (c) Initial  
 175 identification of 7 precipitation objects (different colors) with CCA analysis, and (d)  
 176 Selection of 2 precipitation objects according to object size filtering and morphological  
 177 closing.  
 178

179 Additionally, a modular precipitation approach for the analysis of the precipitation imagery  
 180 was used. For the cases when no precipitation is observed by the PERSIANN-CCS subproduct,  
 181 we switched the precipitation data source to IMERG-early imagery, following a simple  
 182 spatially under-sampling technique. This means that an IMERG-early run cell of size  $0.1 \times 0.1^\circ$   
 183 was directly divided into  $\sim 6.4$  cells with a resolution of  $0.04 \times 0.04^\circ$ , matching the resolution of  
 184 the PERSIANN-CCS subproduct. This modular approach assures that all extreme hydrological  
 185 events are trained with an existent precipitation signal, reducing noise and improving the  
 186 learning process of the further developed runoff models.

## 187 2.3 Classification of precipitation events associated with extreme hydrologic events

188 The hydrometeorological attributes derived from the CCA analysis are used to classify  
189 precipitation events together with their associated runoff response. For this we used the  
190 following two criteria, respectively the extension of the precipitation objects (local and  
191 spatially extensive), and the duration of the precipitation events (short and long). As a result,  
192 by defining extension and duration thresholds we could establish four precipitation event  
193 classes: i) Local and short extreme events (LSE), ii) Local and long-duration extreme events  
194 (LLE), iii) Spatially extensive extreme events (SEE), and iv) Spatially extensive and long-  
195 duration extreme events (SLE).

## 196 2.4 Event-based runoff modeling

197 We developed one runoff model for each precipitation event class and one model without  
198 precipitation discrimination (base model). For this, we used the ML technique known as  
199 Random Forest (RF) for regression. The RF is described in the following subsection. Moreover,  
200 the input feature space to each model was formed with hourly precipitation and runoff, as well  
201 as an indicator of the belonging precipitation class. In addition to current-time precipitation  
202 and runoff information, we used past lag information which is determined according to  
203 statistical correlation analyses: partial- and auto-correlation functions for runoff, and cross-  
204 correlation function for precipitation. The construction of the input feature space was  
205 conducted following the methodology developed in Muñoz et al. (2018), with the purpose to  
206 add only relevant information to the models and improve their efficiencies.

### 207 *3.4.1 Random Forest for regression*

208 Random Forest (RF) is a ML technique of supervised learning where the main idea is to build  
209 multiple decorrelated trees (models), in which the input feature space is related to output(s) by  
210 successively applying a set of hierarchically organized conditions (Breiman, 2001). The key to

211 the RF algorithm is the random selection of resampled datasets from the input feature space  
212 (bagging technique), which assures decorrelation between stochastically formed models.

213 We implemented the RF runoff models through the scikit-learn package for ML in Python®  
214 version 3.7 (Pedregosa et al., 2011). A full explanation of the RF algorithm can be found in  
215 Breiman (2001), and can be summarized as follows:

- 216 i. Construction of each decision tree by randomly selecting several bootstrap samples  
217 from the input feature space. A process known as out-of-bag (OOB) is used for  
218 forming each bootstrap with roughly two-thirds of the input feature space. On one  
219 hand, the OOB process serves to obtain unbiased estimates of the regression, and  
220 on the other hand, it allows to estimate the importance of each feature (predictor)  
221 of the feature space in the tree construction process.
- 222 ii. Optimally splitting of the data selected in step (i) at each node of each tree. This is  
223 done by determining a maximum number of features to perform the best split from  
224 the total number of predictors in the feature space. This also avoids overfitting by  
225 assuring variety and nonexistence of duplicated models.
- 226 iii. Growth of all the trees constructed in step (i) with the splits defined in step (ii) up  
227 to a size defined either by a maximum depth parameter or a minimum number of  
228 samples expected in the final node. Control of the depth of the trees aims to reduce  
229 the structural complexity of the models, leading to model parsimony and noise  
230 reduction.
- 231 iv. Determination of the output of the model as the mean response from all regression  
232 trees.

233 According to Contreras et al. (2021), the most-influencing RF hyperparameters for  
234 hydrological forecasting applications are the number of trees in the forest (`n_trees`), the  
235 maximum number of features to perform the splits of the data (`max_features`), and maximum

236 depth for pruning purposes (`max_depth`). For all runoff models, we determined the optimal  
 237 combinations of hyperparameter following a random grid-search procedure implemented with  
 238 a 10-fold cross-validation process to prevent overfitting. The measure of agreement was  
 239 evaluated according to the coefficient of determination ( $R^2$ ) between simulations and  
 240 observations for the training subsets. Table 1 presents the domain of the selected  
 241 hyperparameters which forms the search space for the optimization task.

242 Table 1. Search space (grid) of the RF runoff models.  
 243

| Hyperparameter            | Domain                                                                                |
|---------------------------|---------------------------------------------------------------------------------------|
| <code>n_trees</code> *    | 40;800;10*                                                                            |
| <code>max_features</code> | <code>n_features</code> , $\text{n\_features}^{(1/2)}$ , $\log_2(\text{n\_features})$ |
| <code>max_depth</code> *  | 40;800;10*                                                                            |

\* Domain defined by min, max, and increment.

#### 244 3.4.2 Model evaluation

245 We used four goodness-of-fit metrics for evaluating the efficiencies of the four runoff models.  
 246 The Nash-Sutcliffe Efficiency (*NSE*) coefficient was set as the reference for measuring and  
 247 comparing the overall model accuracy. To complement the analysis, we relied on the Kling-  
 248 Gupta Efficiency (*KGE*), the Percent Bias (*PBIAS*), and the Root Mean Square Error (*RMSE*)  
 249 metrics. The following equations were used:

$$250 \quad NSE = 1 - \frac{\sum_{i=1}^n (Q_s(i) - Q_o(i))^2}{\sum_{i=1}^n (Q_o(i) - \bar{Q}_o)^2}$$

$$251 \quad KGE = 1 - \sqrt{(r - 1)^2 + (\alpha - 1)^2 + (\beta - 1)^2}$$

$$252 \quad PBIAS = \frac{\sum_{i=1}^n (Q_o - Q_s)}{\sum_{i=1}^n Q_o}$$

$$253 \quad RMSE = \sqrt{\frac{1}{n} \sum_{i=1}^n (Q_s - Q_o)^2}$$

254 where  $n$  is the number of instances,  $Q_s$  is the simulated runoff,  $Q_o$  is observed runoff,  $\bar{Q}_o$  is the  
 255 mean observed runoff,  $\bar{Q}_s$  is the mean simulated runoff,  $r$  is the correlation coefficient between

256  $Q_s$  and  $Q_o$ ,  $\alpha = \frac{\sigma_s}{\sigma_o}$  is the variability ratio,  $\beta = \frac{\overline{Q_s}}{Q_o}$  is the bias ratio, and  $\sigma$  is the standard  
257 deviation.

258 The *NSE* is dimensionless and ranges between  $-\infty$  and 1.0,  $NSE = 1$  being the optimal value.  
259 A limitation of *NSE* is the underestimation of peak flows and overestimation of low flows, in  
260 such cases the *KGE* is suggested (Gupta et al., 2009), with  $KGE = 1$  the optimal value.  
261 Additionally, the optimal value of *PBIAS* is 0, positive values indicate model underestimation  
262 bias and negative values overestimation bias. Finally, *RMSE* measures how model residuals  
263 are spread out from the best fit between simulations and observations, being  $RMSE = 0$  the  
264 optimal value.

### 265 **3. Results**

#### 266 3.1 Determination of nearly independent peak hydrological events

267 The WETSPRO tool for the Jubones basin was calibrated using the following parameters: inter-  
268 event time of 120 hours (i.e., consecutive extreme hydrological events must be separated by a  
269 time frame of at least 5 days), and a maximum ratio of runoff drop down of 0.6 (i.e, runoff,  $q$ ,  
270 drops down in between two consecutive events to a ratio  $\frac{q_{min}}{q_{max}} < 0.6$ ). Moreover, we considered  
271 only events exceeding the 90% quartile values of the runoff time series ( $98.8 \text{ m}^3 \cdot \text{s}^{-1}$ ). With  
272 these criteria, we obtained 55 nearly independent peak hydrological events (see Figure 3a).

#### 273 4.2 Object-based Connected Component Analysis

274 For the 55 peak hydrological events, we firstly retrieved hourly precipitation maps from the  
275 PERSIANN-CCs and the IMERG-early run subproducts. Then, we applied the CCA algorithm  
276 with the precipitation threshold volume of 0.5 mm to derive the meteorological attributes and  
277 classify the precipitation event. The step-by-step application of the CCA algorithm for the map

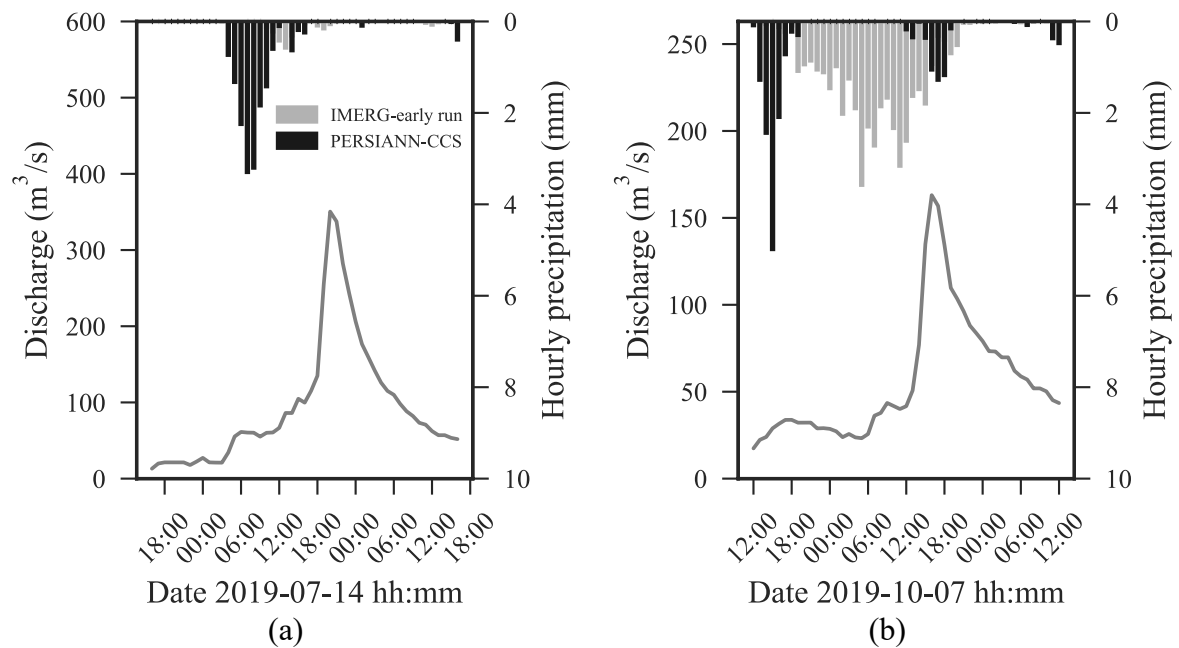
278 corresponding to the PERSIAN-CCS 2021-12-25 05:00 UTC is presented in Figure 4 (see the  
279 Methodology section).

280 CCA results showed that, for 15 extreme hydrological events, there was nearly or even an  
281 inexistent precipitation signal from the PERSIANN-CCS subproduct. For these 15 cases, we  
282 performed the CCA algorithm on the IMERG-early run dataset, and this resulted in a reduction  
283 of 40% of the events without any precipitation signal. In other words, although we used two  
284 precipitation satellite sources, we encountered 9 hydrological events where either no  
285 precipitation at all was observed or any precipitation object was identified according to the  
286 CCA algorithm. Therefore, these events were trimmed off, leaving 46 events available for  
287 further analyses.

288 The validity of the precipitation modular approach is demonstrated in two extreme hydrological  
289 events (see Figure 5). For instance, for the event from 2019-07-13 20:00 to 2019-07-14 20:00  
290 UTC, it seems evident that the highest resolution of the PERSIANN-CCS subproduct leads to  
291 a clearer precipitation-runoff relation when compared to precipitation obtained from the  
292 IMERG-early run subproduct. The opposite happened for the event from 2019-10-07 16:00 to  
293 2019-10-08 16:00 UTC, where the PERSIANN-CCS signal was practically inexistent, and the  
294 IMERG-early run signal was used to relate precipitation with runoff.

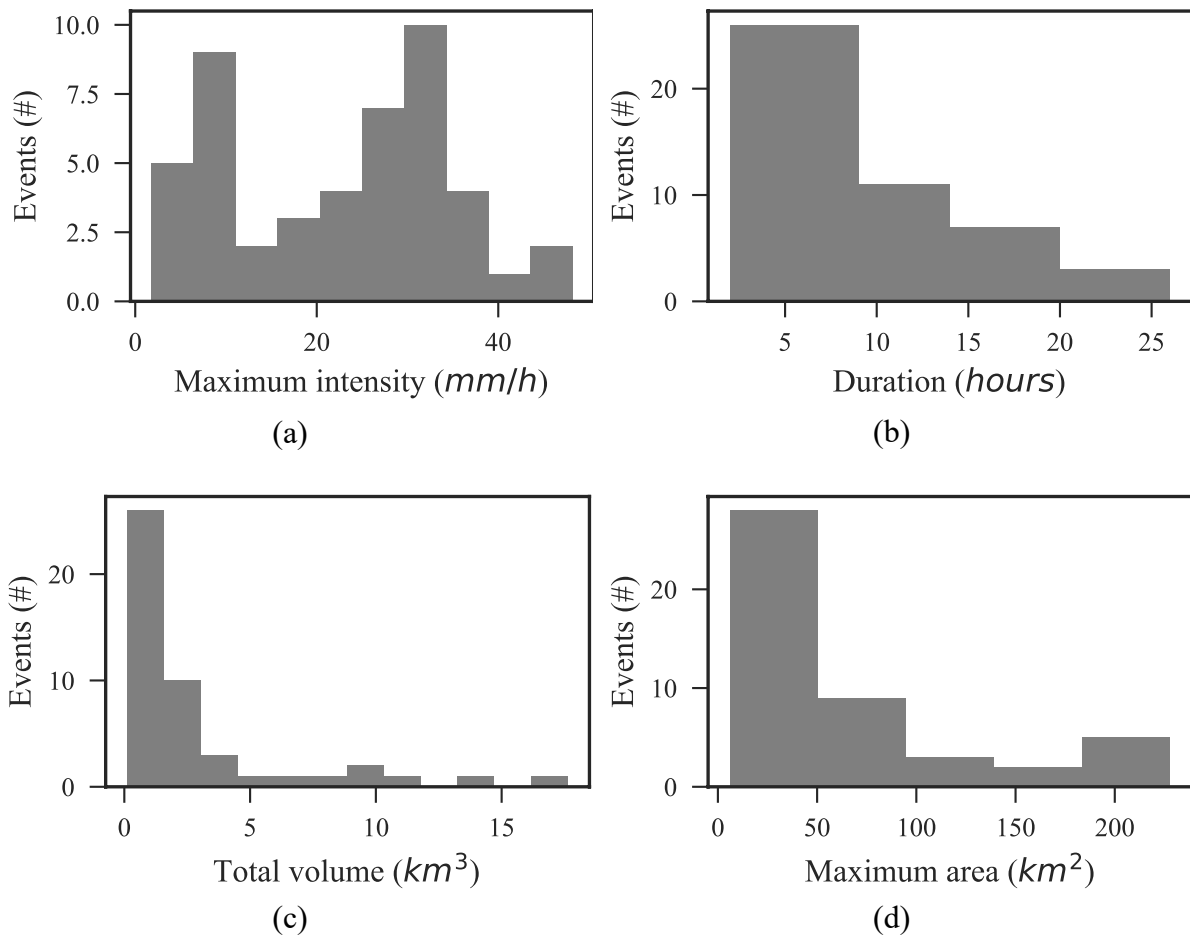
295

296



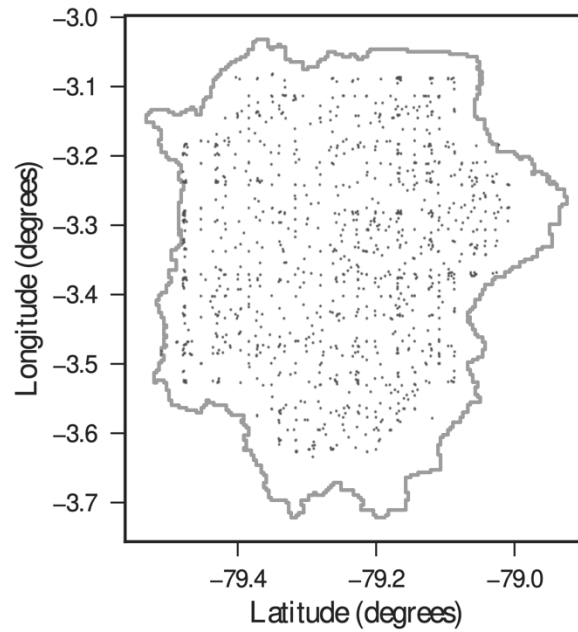
297 Figure 4. Illustration of the precipitation-retrieval modular approach using PERSIANN-CCS  
 298 and IMERG-early run data sources, respectively for the events from (a) 2019-07-13 18:00 to  
 299 2019-07-14 18:00 UTC, and (b) from 2019-10-07 12:00 to 2019-10-08 12:00 UTC.  
 300

301 Moreover, the precipitation objects identified with the CCA algorithm for each one of the 46  
 302 extreme hydrological events were tracked down. From this analysis, the following information  
 303 was retrieved: quantity, localization (centroids) and extension of precipitation objects,  
 304 precipitation duration, total precipitation volume, and precipitation maximum intensity. This  
 305 information is summarized in Figure 6 and served to infer duration and extension thresholds of  
 306 7 hours and 50 km<sup>2</sup>, respectively. These thresholds were used in the following subsection to  
 307 classify the precipitation events.  
 308



309 Figure 5. Meteorological precipitation information retrieved from 47 extreme hydrological  
 310 events: (a) maximum intensity, (b) duration, (c) total volume, and (d) maximum area.  
 311

312 With respect to the localization of precipitation objects within the Jubones basin, centroid  
 313 occurrence appeared to be unaffected by any physical attribute that could be derived for the  
 314 basin (i.e., altitude, land use, etc.). Interestingly, no hotspot of precipitation occurrence was  
 315 detected for the Jubones basin (see Figure 7). This suggests, for instance, that there is no evident  
 316 orographic precipitation enhancement, and that the runoff generation process is rather driven  
 317 by infiltration and saturation mechanisms before precipitation becomes streamflow.

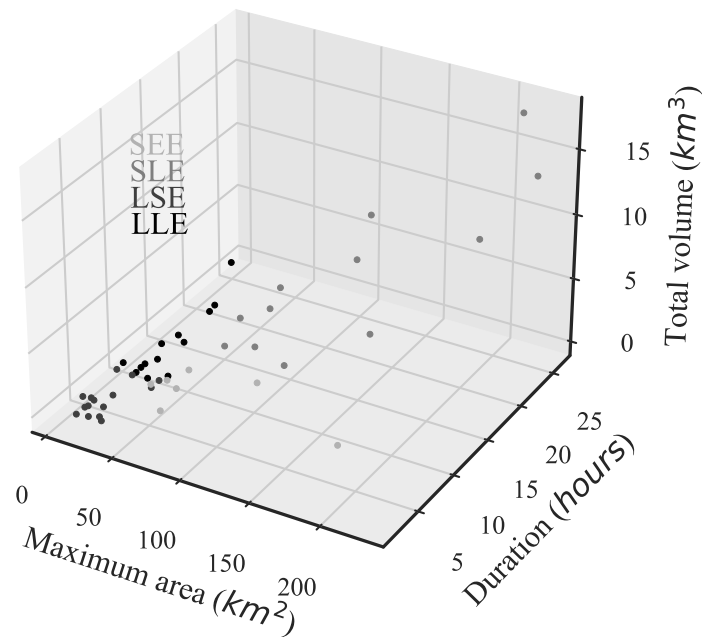


318

319 Figure 6. Localization of precipitation object centroids (green dots) associated with extreme  
320 hydrological events in the Jubones basin.  
321

#### 322 4.3 Classification of precipitation events associated with extreme hydrologic events

323 The combination of duration and extension thresholds of 7 hours and 50 km<sup>2</sup> served to define  
324 four precipitation classes. We determined 24 extreme hydrological events for the LSE  
325 precipitation class, 5 for the LLE, 7 for the SEE, and 10 for the SLE. Figure 8 depicts the visual  
326 discrimination between precipitation classes, from which it is apparent that the majority of  
327 extreme hydrological events occurred as a result of short duration and spatial local (LSE)  
328 precipitation events, and long duration and spatially extensive events (SLE).



329

330 Figure 7. Precipitation classes associated with extreme hydrological events: Local and short  
 331 extreme events (LSE), Local and long-duration extreme events (LLE), Spatially extensive  
 332 extreme events (SEE), and Spatially extensive and long-duration extreme events (SLE).  
 333

#### 334 4.4 Event-based runoff modeling

335 First, we defined the dimension of the input feature space of all extreme runoff models as a  
 336 combination of current time precipitation together with past precipitation and past runoff data  
 337 influencing current rime runoff. In this regard, results from partial- and auto-correlation  
 338 functions for runoff suggest using past lags (hours) from 1 up to 12 lags, with a 95% confidence  
 339 level for both correlation functions. Similarly, the cross-correlation function for precipitation  
 340 determined 13 past lags (hours) of precipitation with correlations higher than 0.2. These results  
 341 are congruent with the concentration-time of the Jubones basin, which was estimated at 11  
 342 hours by averaging the concentration times found with the equations of Giandotti, Johnstone,  
 343 and the U.S. Army Corps of Engineers (equations recommended for the basin area, see de  
 344 Almeida et al. (2014)).

345 Once the input feature space was defined, we constructed RF models for each precipitation  
 346 class and the base model. For the model training and testing of each model, we assigned 70%  
 347 of the events for training and the remaining 30% for testing. For instance, there were 46 events

348 available for the LSE precipitation class; therefore, we assigned 32 events for training and 14  
 349 for testing. Moreover, since the objective was to simulate the hydrographs corresponding to  
 350 each event, we used a time frame of 24 hours before and after peak events. Concerning RF  
 351 hyperparameterization, Table 2 presents the optimized combination of hyperparameters for  
 352 each runoff model. The coefficient of determination between simulations and observations for  
 353 the training subsets of each model was always higher than 0.91.

354

355 Table 2. RF hyperparameterization of extreme runoff models.

| Hyperparameter | None                  | LSE                     | LLE                         | SLE                   | SEE                     |
|----------------|-----------------------|-------------------------|-----------------------------|-----------------------|-------------------------|
| n_trees*       | 300                   | 280                     | 250                         | 300                   | 300                     |
| max_features   | 2100 <sup>(1/2)</sup> | log <sub>2</sub> (2100) | n_features <sup>(1/2)</sup> | 2100 <sup>(1/2)</sup> | log <sub>2</sub> (2100) |
| max_depth*     | 200                   | 200                     | 150                         | 180                   | 200                     |

356

357 Table 3 summarizes the number of events used for developing extreme runoff models, and a  
 358 comparison of the NSE coefficients obtained for each precipitation class and the base model.  
 359 It is apparent from this table that LSE and especially SEE precipitation events are causing  
 360 decay in the overall NSE-value of 0.83 (see also Figures 9b and 9d). Surprisingly, LSE presents  
 361 the majority of extreme hydrological events, and it seems contradictory that for LSE events,  
 362 the higher number of events for training did not result in a higher NSE. This suggests that there  
 363 are physical processes not well represented in the input feature space that disturbs the learning  
 364 process of the RF models, as further discussed.

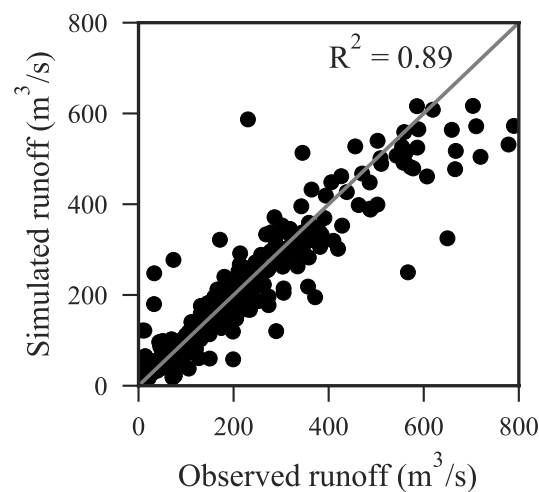
365

366 Table 3. Number of events and efficiencies on test subsets of runoff models specifically  
 367 developed for different precipitation events.

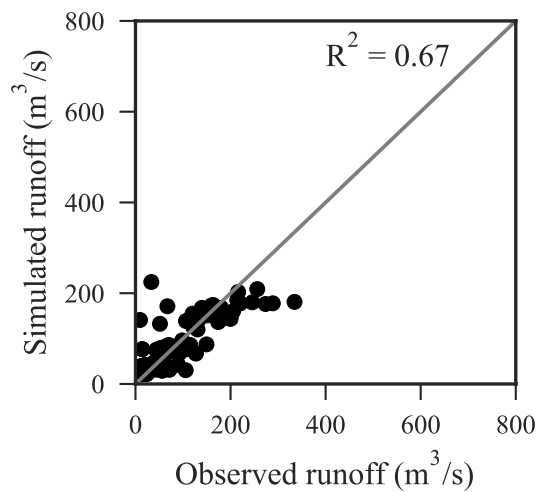
| Precipitation class | # Total Events (Test) | NSE   | KGE   | PBIAS  | RMSE  |
|---------------------|-----------------------|-------|-------|--------|-------|
| None                | 46 (14)               | 0.83  | 0.85  | 4.49   | 55.38 |
| LSE                 | 24 (7)                | 0.67  | 0.71  | -1.45  | 35.00 |
| LLE                 | 5 (2)                 | 0.72  | 0.74  | -23.94 | 41.76 |
| SEE                 | 7 (3)                 | -1.93 | -0.48 | -61.44 | 60.44 |
| SLE                 | 10 (3)                | 0.90  | 0.94  | -2.72  | 69.09 |

368

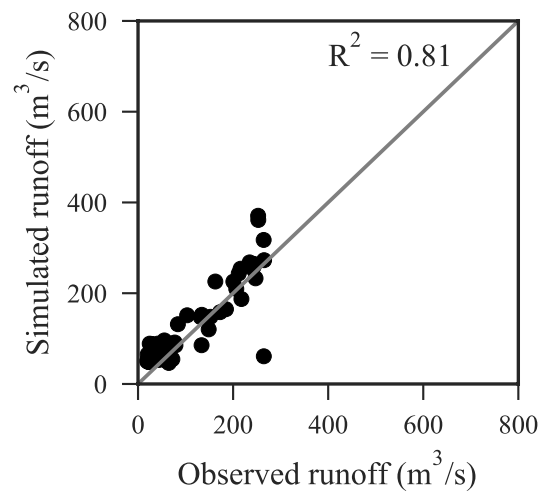
369 From the data in Figure 9, we can infer the spectrum of the runoff magnitudes modeled for  
370 each precipitation class. What is striking from the subfigures in Figure 9 is that regardless of  
371 the spatial extension, short-duration precipitation events (LSE and SEE classes) caused the  
372 lowest extreme runoff magnitudes at the outlet of the Jubones basin. Now, since we developed  
373 models for extreme runoff, we maximized the efficiencies for the highest runoff magnitudes.  
374 Therefore, it is evident that the lowest NSE coefficients for the LSE and SEE classes are found.  
375 Physically, this finding may be explained by the fact that the runoff response of short-duration  
376 events is somehow softened by the infiltration and saturation processes. This means that the  
377 volume of precipitation that becomes streamflow is somehow lower when compared to long-  
378 duration precipitation classes (LLE and SLE). If we now turn to the modeling of all extreme  
379 hydrological events (Figure 9a), we can infer that the learning process is biased towards lower  
380 runoff magnitudes, and the results for the highest magnitudes are more spread out. However,  
381 the bias for long-duration events was reduced by classifying precipitation types before the  
382 modeling task (Figures 9c and 9e).



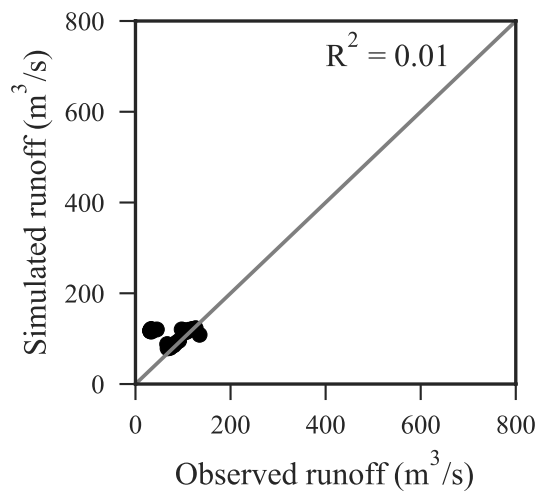
(a)



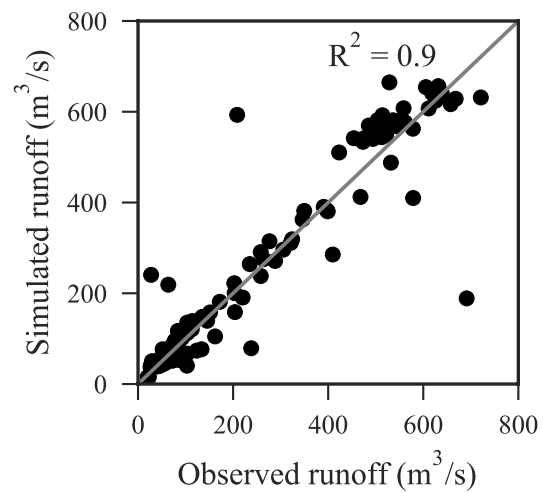
(b)



(c)



(d)



(e)

383

384

385

386

Figure 8. Scatter plot between extreme runoff observations and simulations for (a) No-precipitation event classification, (b) LSE events, (c) LLE events, (d) SEE events, and (e) SLE events.

387

#### 4. Discussion

388

389

390

391

392

In this study, specialized (smart) extreme runoff models were developed for a 3391-km<sup>2</sup> representative basin of the Ecuadorian tropical Andes. The efficiencies of the developed ML models are comparable and outperformed the ones obtained with traditional physically-based models such as HEC-RAS (see the study of Belabid et al. (2019)), wflow-sbm (see Laverde-Barajas et al. (2020)), and the hydrologic-hydraulic HiResFlood-UCI model (see Nguyen et al.

393 (2015)). Particular to this finding is that unlike physically-based models, data-driven runoff  
394 models exploit precipitation satellite data without prior ground validation. Therefore, this study  
395 represents a solution for the cases when ground precipitation networks are scarce or even  
396 inexistent.

397 The specificities of our extreme runoff models were delineated for four precipitation-event  
398 types based on a combination of their duration and spatial extension (LSE, LLE, SEE and SLE).  
399 Developing specialized models served to identify the hidden strong-and-weak points of the  
400 base runoff model without precipitation classification. For instance, this approach could be  
401 used in the study of Belabid et al. (2019), where they obtained, in some cases, unacceptable  
402 runoff efficiencies (negative NSE).

403 For the Jubones basin, the vast majority of extreme hydrological events are the result of local  
404 and short-duration (LSE) precipitation events. In addition, we found that the centroids of LSE-  
405 associated objects were well distributed across the Jubones basin. These results indicate that  
406 small precipitation volumes are concentrated on many small different land use areas,  
407 characterized by a variety of specific runoff generation processes. Therefore, even for a  
408 discriminated LSE precipitation event, multiple precipitation-runoff responses can mislead the  
409 learning process of RF models. This explains the lower model efficiencies of LSE events  
410 (NSE=0.67) in comparison to SLE (0.90) and LLE (0.72) events. The opposite occurred for  
411 the case of long-duration and spatially extensive events (SLE), which were associated with the  
412 most extreme runoff magnitudes. For such events, even though we had less than half of the  
413 events available for LLE, model efficiencies reached the maximum (NSE=0.90). The LLE  
414 runoff model was clearly optimized for extreme runoff magnitudes (KGE=0.94). Physically,  
415 this is explained by the fact that the RF learning process becomes straightforward after a greater  
416 portion of the basin is saturated, and any additional precipitation volume is directly converted

417 into streamflow. The major difficulty comes from the modeling of extreme runoff triggered by  
418 spatially-extensive and short-duration precipitation events (SEE).  
419 The efficiencies of the developed and tested models highlighted the advantage of developing  
420 specialized extreme runoff models but also revealed the need to include additional information  
421 on antecedent soil saturation and its dynamic along with extreme hydrological events. This is  
422 particularly required for short-duration precipitation events (SEE and LSE), where the runoff  
423 generation process is governed by the antecedent saturation state of the basin. Foregoing is the  
424 reason why short-duration and non-extreme precipitation intensities can trigger extreme  
425 hydrological events. Given this, we encourage the approach employed by Massari et al. (2018)  
426 where they used satellite soil moisture observations to improve extreme runoff forecasting.  
427 Moreover, unveiling the limitations of runoff modeling for the Jubones basin opens the path  
428 for future research focused on exploring additional ML algorithms. We recommend, for  
429 instance, exploration of additional ML algorithms for the modeling of LSE and SEE events,  
430 and to come up with a superior model consisting of an ensemble of specialized runoff models.

## 431 **5. Conclusions**

432 This study exploits the possibility of using two near-real-time satellite precipitation sources  
433 (without ground validation) for the development of smart extreme runoff models for a 3391-  
434 km<sup>2</sup> basin. Smart models are characterized by the use of a ML algorithm with prior data  
435 assimilation enhancement under hydrometeorological criteria. For dealing with complex  
436 precipitation-runoff response and the optimization of the runoff model efficiency a  
437 straightforward feature engineering methodology was used. The major finding emerging from  
438 this study is that improvement of the representation of precipitation maximizes the efficiency  
439 of extreme runoff models. In addition, precipitation discrimination also served to unveil the  
440 precipitation-runoff scenarios misleading the learning process of RF extreme models.

441 In general, we found that the spatial extension of precipitation events made no significant  
442 difference in the learning process of RF models when they occurred for long-duration periods.  
443 In fact, these particular events produced the highest runoff magnitudes at the outlet of the basin.  
444 Physically, the success in modeling such precipitation events is attributed to a clear  
445 precipitation-runoff signal resulting from a gradual soil saturation process before precipitation  
446 is turned into runoff. This signal served to improve the learning process of RF models by  
447 reducing noise and maximizing model efficiencies. In terms of input data, the present study  
448 intentionally used and tested two near-real-time precipitation satellite sources, the PERSIAN-  
449 CCS and IMERG-early run subproducts. We used a modular framework of precipitation data  
450 acquisition that reduced 40% of precipitation events with nearly- or even inexistent  
451 precipitation signal.

452 All in all, the knowledge gained from the functioning of the basin, the proposed feature  
453 engineering methodology, and the evaluation of nearly-real-time satellite precipitation sources  
454 provides hydrologists with the tools for the future development of real-time runoff forecasting  
455 models. In addition, this study can be used to assist decision-makers in the fields of flood  
456 forecasting, water resources management, optimization of hydropower generation, and many  
457 more.

## 458 **References**

- 459 Belabid, N., Zhao, F., Brocca, L., Huang, Y., Tan, Y., 2019. Near-real-time flood forecasting  
460 based on satellite precipitation products. *Remote Sens.* 11, 252.
- 461 Biau, G., Scornet, E., 2016. A random forest guided tour. *Test* 25, 197–227.  
462 <https://doi.org/10.1007/s11749-016-0481-7>
- 463 Bontempi, G., Taieb, S. Ben, Le Borgne, Y.-A., 2012. Machine Learning Strategies for Time  
464 Series Forecasting., in: *EBISS*. pp. 62–77.
- 465 Breiman, L., 2001. Random forests. *Mach. Learn.* 45, 5–32.  
466 <https://doi.org/10.1023/A:1010933404324>
- 467 Chang, L.-C., Chang, F.-J., Yang, S.-N., Kao, I., Ku, Y.-Y., Kuo, C.-L., Amin, I., others,  
468 2019. Building an Intelligent Hydroinformatics Integration Platform for Regional Flood  
469 Inundation Warning Systems.

- 470 Clark, M.P., Bierkens, M.F.P., Samaniego, L., Woods, R.A., Uijlenhoet, R., Bennett, K.E.,  
471 Pauwels, V.R.N., Cai, X., Wood, A.W., Peters-lidard, C.D., 2017. The evolution of  
472 process-based hydrologic models : historical challenges and the collective quest for  
473 physical realism 3427–3440.
- 474 Contreras, P., Orellana-Alvear, J., Muñoz, P., Bendix, J., Célleri, R., 2021. Influence of  
475 Random Forest Hyperparameterization on Short-Term Runoff Forecasting in an Andean  
476 Mountain Catchment. *Atmosphere (Basel)*. 12, 238.
- 477 Davis, C., Brown, B., Bullock, R., 2006. Object-based verification of precipitation forecasts.  
478 Part I: Methodology and application to mesoscale rain areas. *Mon. Weather Rev.* 134,  
479 1772–1784.
- 480 de Almeida, I.K., Almeida, A.K., Anache, J.A.A., Steffen, J.L., Alves Sobrinho, T., 2014.  
481 Estimation on time of concentration of overland flow in watersheds: A review.  
482 *Geociencias* 33, 661–671.
- 483 der Walt, S., Schönberger, J.L., Nunez-Iglesias, J., Boulogne, F., Warner, J.D., Yager, N.,  
484 Gouillart, E., Yu, T., 2014. scikit-image: image processing in Python. *PeerJ* 2, e453.
- 485 Galelli, S., Castelletti, A., 2013. Assessing the predictive capability of randomized tree-based  
486 ensembles in streamflow modelling. *Hydrol. Earth Syst. Sci.* 17, 2669–2684.
- 487 Gupta, H. V, Kling, H., Yilmaz, K.K., Martinez, G.F., 2009. Decomposition of the mean  
488 squared error and NSE performance criteria: Implications for improving hydrological  
489 modelling. *J. Hydrol.* 377, 80–91.
- 490 Gutiérrez-Jurado, K.Y., Partington, D., Batelaan, O., Cook, P., Shanafield, M., 2019. What  
491 triggers streamflow for intermittent rivers and ephemeral streams in low-gradient  
492 catchments in Mediterranean climates. *Water Resour. Res.* 55, 9926–9946.
- 493 Hong, Y., Hsu, K.-L., Sorooshian, S., Gao, X., 2004. Precipitation estimation from remotely  
494 sensed imagery using an artificial neural network cloud classification system. *J. Appl.*  
495 *Meteorol.* 43, 1834–1853.
- 496 Hong, Y., Tang, G., Ma, Y., Huang, Q., Han, Z., Zeng, Z., Yang, Y., Wang, C., Guo, X.,  
497 2019. Remote sensing precipitation: Sensors, retrievals, validations, and applications.  
498 *Obs. Meas. Li, X., Vereecken, H., Eds* 1–23.
- 499 Hsu, K., Gao, X., Sorooshian, S., Gupta, H. V, 1997. Precipitation estimation from remotely  
500 sensed information using artificial neural networks. *J. Appl. Meteorol.* 36, 1176–1190.
- 501 Huffman, G.J., Bolvin, D.T., Braithwaite, D., Hsu, K., Joyce, R., Xie, P., Yoo, S.-H., 2015.  
502 NASA global precipitation measurement (GPM) integrated multi-satellite retrievals for  
503 GPM (IMERG). *Algorithm Theor. Basis Doc.* Version 4, 26.
- 504 Laverde-Barajas, M., Corzo, G., Bhattacharya, B., Uijlenhoet, R., Solomatine, D.P., 2019.  
505 Spatiotemporal analysis of extreme rainfall events using an object-based approach, in:  
506 *Spatiotemporal Analysis of Extreme Hydrological Events*. Elsevier, pp. 95–112.
- 507 Laverde-Barajas, M., Perez, G.A.C., Chishtie, F., Poortinga, A., Uijlenhoet, R., Solomatine,  
508 D.P., 2020. Decomposing satellite-based rainfall errors in flood estimation:  
509 Hydrological responses using a spatiotemporal object-based verification method. *J.*  
510 *Hydrol.* 591, 125554.
- 511 Li, B., Yang, G., Wan, R., Dai, X., Zhang, Y., 2016. Comparison of random forests and other  
512 statistical methods for the prediction of lake water level: a case study of the Poyang  
513 Lake in China. *Hydrol. Res.* 47, 69–83. <https://doi.org/10.2166/nh.2016.264>

- 514 Li, J., Hsu, K.-L., AghaKouchak, A., Sorooshian, S., 2016. Object-based assessment of  
515 satellite precipitation products. *Remote Sens.* 8, 547.
- 516 Li, M., Zhang, Y., Wallace, J., Campbell, E., 2020. Estimating annual runoff in response to  
517 forest change: A statistical method based on random forest. *J. Hydrol.*  
518 <https://doi.org/10.1016/j.jhydrol.2020.125168>
- 519 Massari, C., Camici, S., Ciabatta, L., Brocca, L., 2018. Exploiting satellite-based surface soil  
520 moisture for flood forecasting in the Mediterranean area: State update versus rainfall  
521 correction. *Remote Sens.* 10, 292.
- 522 Mosavi, A., Ozturk, P., Chau, K.W., 2018. Flood prediction using machine learning models:  
523 Literature review. *Water (Switzerland)* 10, 1–40. <https://doi.org/10.3390/w10111536>
- 524 Muñoz, P., Orellana-Alvear, J., Célleri, R., 2021. Application of a Machine Learning  
525 Technique for Developing Short-Term Flood and Drought Forecasting Models in  
526 Tropical Mountainous Catchments, in: *Integrated Research on Disaster Risks*. Springer,  
527 pp. 11–35.
- 528 Muñoz, P., Orellana-Alvear, J., Willems, P., Célleri, R., 2018. Flash-flood forecasting in an  
529 andean mountain catchment-development of a step-wise methodology based on the  
530 random forest algorithm. *Water (Switzerland)* 10. <https://doi.org/10.3390/w10111519>
- 531 Nguyen, P., Sellars, S., Thorstensen, A., Tao, Y., Ashouri, H., Braithwaite, D., Hsu, K.,  
532 Sorooshian, S., 2014. Satellites track precipitation of super typhoon Haiyan. *Eos, Trans.*  
533 *Am. Geophys. Union* 95, 133–135.
- 534 Nguyen, P., Thorstensen, A., Sorooshian, S., Hsu, K., AghaKouchak, A., 2015. Flood  
535 forecasting and inundation mapping using HiResFlood-UCI and near-real-time satellite  
536 precipitation data: The 2008 Iowa flood. *J. Hydrometeorol.* 16, 1171–1183.
- 537 Orellana-Alvear, J., Célleri, R., Rollenbeck, R., Muñoz, P., Contreras, P., Bendix, J., 2020.  
538 Assessment of Native Radar Reflectivity and Radar Rainfall Estimates for Discharge  
539 Forecasting in Mountain Catchments with a Random Forest Model. *Remote Sens.* 12,  
540 1986.
- 541 Papacharalampous, G.A., Tyralis, H., 2018. Evaluation of random forests and Prophet for  
542 daily streamflow forecasting 201–208.
- 543 Pedregosa, F., Varoquaux, G., Gramfort, A., Michel, V., Thirion, B., Grisel, O., Blondel, M.,  
544 Prettenhofer, P., Weiss, R., Dubourg, V., Vanderplas, J., Passos, A., Cournapeau, D.,  
545 Brucher, M., Perrot, M., Duchesnay, É., 2011. Scikit-learn: Machine learning in Python.  
546 *J. Mach. Learn. Res.*
- 547 Peña-Barragán, J.M., Ngugi, M.K., Plant, R.E., Six, J., 2011. Object-based crop identification  
548 using multiple vegetation indices, textural features and crop phenology. *Remote Sens.*  
549 *Environ.* 115, 1301–1316.
- 550 Sakib, S., Ghebreyesus, D., Sharif, H.O., 2021. Performance Evaluation of IMERG GPM  
551 Products during Tropical Storm Imelda. *Atmosphere (Basel)*. 12, 687.
- 552 Sorooshian, S., Nguyen, P., Sellars, S., Braithwaite, D., AghaKouchak, A., Hsu, K., 2014.  
553 Satellite-based remote sensing estimation of precipitation for early warning systems.  
554 *Extrem. Nat. hazards, disaster risks Soc. Implic.* 1, 99.
- 555 Tang, G., Long, D., Hong, Y., 2016. Systematic anomalies over inland water bodies of High  
556 Mountain Asia in TRMM precipitation estimates: No longer a problem for the GPM  
557 era? *IEEE Geosci. Remote Sens. Lett.* 13, 1762–1766.

- 558 Tyralis, H., Papacharalampous, G., Langousis, A., 2019. A brief review of random forests for  
559 water scientists and practitioners and their recent history in water resources. *Water*  
560 (Switzerland). <https://doi.org/10.3390/w11050910>
- 561 Vogels, M.F.A., de Jong, S.M., Sterk, G., Wanders, N., Bierkens, M.F.P., Addink, E.A.,  
562 2020. An object-based image analysis approach to assess irrigation-water consumption  
563 from MODIS products in Ethiopia. *Int. J. Appl. Earth Obs. Geoinf.* 88, 102067.
- 564 Wang, Z., Lai, C., Chen, X., Yang, B., Zhao, S., Bai, X., 2015. Flood hazard risk assessment  
565 model based on random forest. *J. Hydrol.* 527, 1130–1141.  
566 <https://doi.org/10.1016/j.jhydrol.2015.06.008>
- 567 Willems, P., 2009. A time series tool to support the multi-criteria performance evaluation of  
568 rainfall-runoff models. *Environ. Model. Softw.* 24, 311–321.
- 569 Young, P.C., 2002. Advances in real-time flood forecasting. *Philos. Trans. R. Soc. London.*  
570 *Ser. A Math. Phys. Eng. Sci.* 360, 1433–1450.
- 571
- 572
- 573